Tissue and Cell 101 (2026) 103482

Contents lists available at ScienceDirect

Tissue and Cell

journal homepage: www.elsevier.com/locate/tice

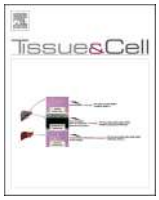

Active whitening of human SGBS adipocytes is associated with coordinated AMPK–HIF–autophagy signalling and mitochondrial remodelling

MONICA COLITTI [a,*,1], Andrea Venerando [b,2], Giulia Polacchini [b,3]

[a] Department of Agricultural, Food, Environmental and Animal Sciences, University of Udine, Italy
[b] University of Udine

ARTICLE INFO

Keywords:
SGBS cells
adipocyte whitening
late differentiation
mitochondrial remodelling
AMPK–HIF–autophagy

ABSTRACT

Adipocyte whitening is a late-stage phenotypic transition that follows transient browning; however, its cellular and molecular basis remains incompletely understood. In particular, it is debated whether whitening reflects a passive loss of thermogenic identity or an actively regulated adaptive state. Late-stage whitening was investigated in human Simpson-Golabi-Behmel syndrome (SGBS) adipocytes using an integrated approach combining quantitative mitochondrial morphology, lipid droplet remodelling, transcriptomics, protein analyses, and network-based bioinformatics. Whitening was characterised by coordinated suppression of thermogenic and oxidative gene programmes, together with enrichment of pathways associated with AMPK signalling, hypoxia response, and autophagy. Quantitative imaging analyses revealed stabilisation and remodelling of the mitochondrial network, with features consistent with mitochondrial quality control rather than degenerative loss of function. Transcriptomic and network analyses further supported the enrichment of autophagy-related processes and —adaptive signalling pathways during the late stages of differentiation. Overall, these findings indicate that adipocyte whitening is an actively regulated adaptive cellular state, integrating mitochondrial structural remodelling with metabolic and stress-responsive signalling. These results provide a conceptual framework for understanding adipocyte phenotypic plasticity during late differentiation.

1. Introduction

White adipocytes play a central role in systemic energy homeostasis (Farmer, 2006). However, excessive adipocyte hypertrophy or hyperplasia, along with impaired endocrine and metabolic functions, are closely linked to obesity and related disorders, including type 2 diabetes,

Abbreviations: ACAD8, Acyl-CoA dehydrogenase family member 8; ACADSB, Acyl-CoA dehydrogenase, short/branched chain; ACCA1, Acetyl-CoA carboxylase alpha; ACSL4, Acyl-CoA Synthetase Long-Chain Family Member 4; ALOX5AP, Arachidonate 5-Lipoxygenase Activating Protein; BECN1, Beclin 1; CIDEA, Cell death-inducing DFFA-like effector A; CPT2, Carnitine palmitoyltransferase 2; CYFIP1, Cytoplasmic FMR1-interacting protein 1; ECH1, Enoyl-CoA hydratase 1, peroxisomal; EHHADH, Enoyl-CoA hydratase and 3-hydroxyacyl CoA dehydrogenase; ELOVL3, ELOVL fatty acid elongase 3; ETFB, Electron transfer flavoprotein subunit beta; ETFDH, Electron transfer flavoprotein dehydrogenase; FTH1, Ferritin Heavy Chain 1; GAPDH, Glyceraldehyde-3-phosphate dehydrogenase; GPX, Glutathione peroxidase 4; HO-1/ HMOX1, Heme oxygenase 1; HSDL2, Hydroxysteroid dehydrogenase like 2; LAMP2, Lysosomal associated membrane protein 2; LC3B-II, Microtubule-associated protein 1 light chain 3 beta; MRPL1, Mitochondrial ribosomal protein L1; MRPL21, Mitochondrial ribosomal protein L21; MRPL24, Mitochondrial ribosomal protein L24; MRPL32, Mitochondrial ribosomal protein L32; MRPL36, Mitochondrial ribosomal protein L36; MRPS12, Mitochondrial ribosomal protein S12; MRPS14, Mitochondrial ribosomal protein S14; MRPS15, Mitochondrial ribosomal protein S15; MRPS18C, Mitochondrial ribosomal protein S18C; MTIF2, Mitochondrial translational initiation factor 2; NBR1, Neighbor of BRCA1 gene 1; P62/SQSTM1, Sequestosome 1; PAK4, P21 RAC1 activated kinase 4; SART1, Squamous cell carcinoma antigen recognized by T cells 1; SCP2, Sterol carrier protein 2; SLC2A1, Solute Carrier Family 2 Member 1; SLC7A11, Solute Carrier Family 7 Member 11; UCP1, Uncoupling protein 1; ULK1, Unc-51 like autophagy activating kinase 1; USP39, Ubiquitin specific peptidase 39; WIPI1, WD repeat domain, phosphoinositide interacting 1.

* Corresponding author.
E-mail addresses: monica.colitti@uniud.it (M. COLITTI), andrea.venerando@uniud.it (A. Venerando), giulia.polacchini@uniud.it, polacchini.giulia@spes.uniud.it (G. Polacchini).
[1] 0000–0002-1775–3880
[2] 0000–0003-0379–2309
[3] 0000–0001-6984–8198

https://doi.org/10.1016/j.tice.2026.103482
Received 3 February 2026; Received in revised form 17 March 2026; Accepted 18 March 2026
Available online 22 March 2026

cardiovascular disease, and hypertension (Romero-Corral et al., 2008). The conversion of white adipose tissue (WAT) into thermogenic brown adipose tissue (BAT) has therefore emerged as a promising therapeutic strategy to counteract metabolic disease (Cannon and Nedergaard, 2017). The identification of metabolically active BAT in adult humans has further highlighted the importance of adipocyte plasticity (Cypess et al., 2009). Beyond classical brown adipocytes, beige adipocytes arise within WAT depots through browning, underscoring the need to characterise the mechanisms regulating adipocyte phenotypic transitions.

In vitro adipocyte models are essential for investigating adipogenesis, insulin sensitivity, adipokine secretion, and thermogenic programming. Although murine cell lines and human stromal vascular fractions are commonly used, their utility is limited by donor variability and replicative senescence. Simpson–Golabi–Behmel syndrome (SGBS) cells, by contrast, retain robust adipogenic capacity for up to 50 passages and provide a reliable human model for studying adipocyte biology (Wabitsch et al., 2001). Sustained PPARγ activation promotes the acquisition of beige features in SGBS adipocytes, including the development of multilocular lipid droplets and activation of thermogenic genes such as UCP1, CIDEA, and ELOVL3 (Klusóczki et al., 2019). Transcriptomic profiling of early differentiation stages further revealed induction of extracellular matrix and oxidative stress-related genes associated with beige identity (Colitti et al., 2022), followed by a progressive reversion towards a white adipocyte programme (Halbgebauer et al., 2020).

Several cellular mechanisms have been proposed to contribute to the beige-to-white transition, although their relative contributions in human adipocytes remain unclear. Autophagy, particularly mitophagy, may facilitate mitochondrial remodelling and loss of thermogenic activity (Altshuler-Keylin et al., 2016; Lu et al., 2018; Szatmári-Tóth et al., 2020). Altered oxygen availability and HIF-1α activation have been linked to changes in thermogenic gene expression and adipose tissue remodelling (Jun et al., 2017; Shimizu et al., 2014). Moreover, ferroptosis-related lipid peroxidation has been implicated in adipocyte plasticity, albeit in a highly context-dependent manner (Wang et al., 2025). Collectively, these findings indicate that whitening integrates multiple pathways that coordinate mitochondrial function, lipid handling and transcriptional identity. However, whether whitening represents a passive loss of function or an actively regulated metabolic adaptation in human adipocytes remains unresolved. Here, we address this gap by applying RNA sequencing to SGBS adipocytes after the peak of their browning phenotype (day 14) and at a later differentiation stage (day 28) to identify genes and pathways associated with the transition towards a white-like phenotype.

2. Materials and methods

2.1. Chemicals and culture media

Dulbecco's modified Eagle medium (DMEM)/F-12 (1:1), supplemented with L-glutamine, 15 mM 4-(2-hydroxyethyl)-1-piperazineethanesulfonic acid (HEPES), fetal bovine serum (FBS), and penicillin–streptomycin, was purchased from Gibco (Thermo Fisher Scientific Inc. Waltham, Massachusetts). TRIzol reagent, the PureLink RNA Mini Kit, and the SuperScript III One-Step RT-PCR System with Platinum Taq DNA Polymerase were obtained from Invitrogen (Thermo Fisher Scientific Inc.). Rosiglitazone was purchased from Cayman Chemical. All other chemicals not otherwise specified were obtained from Sigma-Aldrich.

2.2. Cell culture

Human Simpson–Golabi–Behmel syndrome (SGBS) cells were kindly provided by Prof. M. Wabitsch (University of Ulm). Cells were cultured in DMEM/F-12 supplemented with 10% fetal bovine serum (FBS), 3.3 mM biotin, 1.7 mM pantothenate, and 1% penicillin–streptomycin at 37 °C in a humidified atmosphere containing 5% CO_2. Differentiation was induced at confluence using serum-free growth medium supplemented with 10 μg/mL transferrin, 0.2 nM triiodothyronine (T3), 250 nM hydrocortisone, 20 nM human insulin, 25 nM dexamethasone, 250 μM 3-isobutyl-1-methylxanthine (IBMX), and 2 μM rosiglitazone (day 0). After 4 days, the differentiation medium was replaced with a maintenance medium consisting of serum-free growth medium supplemented with 10 μg/mL transferrin, 0.2 nM T3, 250 nM hydrocortisone, and 20 nM human insulin. Fresh maintenance medium was replaced every 4 days. The cells were analysed during differentiation on day 0 (D0), day 2 (D02), day 14 (D14), day 20 (D20) and day 28 (D28).

2.3. MitoTracker™ staining and Mitochondrial morphology analysis

SGBS cells were plated in μ-Slide 8-well IbiTreat chambers (Ibidi GmbH, Germany) and cultured and differentiated according to the protocol described above. At the indicated time points, the culture medium was aspirated and the cells were incubated with 100 nM MitoTracker™ diluted in maintenance medium. Staining was performed for 30 min at 37 °C in a humidified atmosphere containing 5% CO_2. The cells were then washed with phosphate-buffered saline (PBS) and fixed in 2% formalin prepared in PBS for 15 min at room temperature. After fixation, samples were washed three times with PBS and counterstained with Hoechst at a final working concentration of 5 μg/mL in PBS for 10 min at room temperature. Fluorescence images were acquired using an Axio Observer Z1 inverted microscope (Carl Zeiss) equipped with D-PLAN Neofluar objectives (numerical aperture 0.75), an Infinity Colour-Corrected System (ICS), an AxioCam camera, and ZEN Blue software. Excitation/emission filter sets of 550/605 nm and 390/460 nm were used for MitoTracker™ and Hoechst, respectively.

To analyse and classify mitochondria in SGBS cells at different stages of differentiation, standard fluorescence microscopy images were processed using the Mitochondrial Analyzer software, which applies an adaptive thresholding approach, in combination with the open-source image analysis platform ImageJ/Fiji (Chaudhry et al., 2020). Scaling was set for magnification, and the global checkbox in the Set Scaling dialogue box was selected. After 2D threshold optimisation, the images were thresholded with a block size of 1250 μm and a C value of 5. The same images were then further processed using the Micro2P tool, which analysed mitochondrial fragmentation as previously validated in CHO-K1 cells (Peng et al., 2011). At least 14 independent fields of view per time point (D02, D14, D20, D28) were analysed, obtained from two independent differentiation experiments, which represent the biological replicates. Quantitative parameters were calculated per image, and images were treated as the analytical unit for statistical comparison.

The Mitochondrial Analyzer tool was used to quantify mitochondrial number and morphological parameters, including the mean aspect ratio (an indicator of mitochondrial elongation) and the mean form factor (reflecting the transition from rounded to filamentous structures). Indices of mitochondrial network connectivity were also determined, such as the number of branches, total branch length normalised to mitochondrial number, average branch length, and mean branch diameter. Finally, the MicroP software was used to classify the different morphological subtypes into small globules (round-shaped mitochondria probably formed by fission), simple tubules (straight, elongated mitochondria without branching), and branched tubules (complex, interconnected mitochondria with a net-like structure).

2.4. Lipid droplets morphology and quantification

Cells seeded in μ-slide 8 well IbiTreat chambers were fixed with 2% formalin in PBS at room temperature (RT) for 15 min, washed three times with PBS and then incubated with Bodipy™ 493/503 at a final working concentration of 1 μg/mL in PBS to specifically label lipid droplets. Incubation was carried out at RT for 45 min. Cells were then washed three times with PBS and finally stained with Hoechst at a final

concentration of 5 μg/mL. Images were acquired using the fluorescence microscope Axio Observer Z1 equipped with AxioCam and Zen blue software (Carl Zeiss, Jena, Germany). The filters were set at 470/525 nm for FITC, and 390/460 nm for Hoechst.

Lipid droplet (LD) area was quantified using the MRI_Lipid Droplets tool, an ImageJ macro specifically designed for lipid droplet analysis (Su et al., 2022). LDs were segmented automatically from Bodipy™ -stained images using a fixed threshold. Quantification was performed at the level of individual fields of view (one data point = one image). For each field, the percentage of the total area occupied by lipid droplets (% LD area), and the median Feret diameter (μm) calculated among all LDs within that field were measured. Between 7 and 25 independent fields of view per time point were analysed, obtained from two independent differentiation experiments, which represent the biological replicates.

2.5. RNA extraction and sequencing

SGBS cells were seeded onto Petri dishes and differentiated for the indicated times, as described above. The experiment included two biological replicates.

After removing the culture medium and washing with PBS, 1 mL per 10 cm^2 of TRIzol reagent was added to each plate and pipetted repeatedly. Total RNA was isolated using the PureLink RNA Mini Kit according to the manufacturer's protocol. RNA concentration was determined spectrophotometrically using a NanoDrop 1000 instrument (Thermo Fisher Scientific Inc., Wilmington, Delaware), and sample purity was verified by absorbance ratios, which ranged from 1.8 to 1.9. RNA integrity was assessed by visualising the 18S and 28S ribosomal RNA bands after electrophoresis on a 1% agarose gel containing GelRed. Additionally, the integrity of the extracted RNA was further confirmed by assessing β-actin expression as an internal control.

High-quality total RNA was subsequently processed for deep sequencing analysis. RNA quantity and integrity were assessed using the Agilent 2100 Bioanalyzer (Agilent Technologies), and only samples with an RNA integrity number (RIN) greater than 8.0 were used for sequencing. RNA sequencing (RNA-seq) was performed using the Illumina Genome Analyzer platform (Illumina) to profile mRNA expression in eight human cell line samples. For library preparation, 2–4 μg of total RNA per sample was used. Total RNA was reverse-transcribed into double-stranded cDNA, digested with *Nla*III, and ligated to Illumina-specific adapters containing a MmeI restriction site. Following MmeI digestion, a second Illumina adapter with a degenerate two-base 3′ overhang was ligated. Sequencing reads were aligned to the human reference genome GRCh38 using STAR alignment software. Raw sequencing data have been deposited in the NCBI Sequence Read Archive under BioProject ID PRJNA1390728.

2.6. Data processing

Raw data were uploaded to the R package Differential Expression and Pathway analysis (iDEP2.1), a web-based tool available at http://ge-lab.org/idep/ (Ge et al., 2018; Ge, 2021). Genes with very low expression were filtered out, retaining only those with a minimum of 1 count per million (CPM) in at least two libraries. iDEP internally normalised the data to CPM and applied a $\log_2$ transformation with a pseudocount (c = 4). The DESeq2 package was then used to identify differentially expressed genes (DEGs) at day 28 of differentiation compared to days 0, 2, 14 and 20, using a false discovery rate (FDR) threshold of < 0.05 and $\log_2$fold-change $> |1.0|$. Lists of differentially expressed genes for all pairwise comparisons are provided in Table S1.

Multivariate analyses, including heat map visualisation, PCA, k-means clustering, and functional enrichment, were conducted using iDEP 2.1. Enriched biological processes and pathways associated with differentially expressed genes were identified through gene set enrichment analysis based on significant GO terms (Ashburner et al., 2000), and KEGG pathway annotations (Kanehisa and Goto, 2000).Full enrichment outputs are reported in Tables S2–S4. Venn diagrams were generated using the web tool available at http://bioinformatics.psb.ugent.be/webtools/Venn/.

2.7. Protein–protein interaction (PPI) network construction, module and functional enrichment analyses

Protein–protein interaction (PPI) networks were generated using the STRING database, with a minimum interaction confidence score of 0.4. Network visualisation and topological analyses were performed using Cytoscape (version 3.10.3).

Differentially expressed genes (DEGs) from the most relevant pairwise comparisons were further analysed using the Molecular Complex Detection (MCODE) plug-in (parameters: degree cutoff = 2, node score = 0.2, k-core = 2, maximum depth = 100) to identify highly connected modules within the networks.

The most significant MCODE clusters were then analysed with the CytoHubba plug-in to identify hub genes. The Maximal Clique Centrality (MCC) algorithm was used to rank nodes according to network centrality, providing high sensitivity and accuracy in detecting essential hubs in biological systems (Chin et al., 2014).

Functional annotation of genes in significant clusters and hub modules was carried out using Metascape, integrating GO terms, KEGG and Reactome pathways, and UniProt Keyword enrichment. Significant terms were prioritised based on FDR values and classified into biological process, cellular component, molecular function, and pathway categories. Enrichment analyses were applied to differentially expressed genes and to MCODE clusters.

Summary results for network-derived modules are shown in Table S6, and full enrichment results are reported in Table S7.

2.8. BATLAS webtool analysis

The thermogenic potential of adipocytes, expressed as brown adipose tissue (BAT) content, was quantified using the BATLAS web-based tool. BATLAS uses hierarchical clustering algorithms to infer browning capacity from mouse and human RNA-seq datasets (Perdikari et al., 2018). The relative proportion of brown adipocytes at different stages of differentiation was estimated for each sample based on normalised read counts.

2.9. Total protein extraction and Western blot analysis

On the specified day of differentiation, SGBS cells were scraped from 10 cm Petri dishes using a cell scraper, collected in PBS, and centrifuged at 3000 × g for 10 min. Cells were lysed in ice-cold RIPA buffer containing a protease inhibitor cocktail (Roche, Switzerland), 1 mM sodium orthovanadate, and 1 mM sodium fluoride to inhibit protein phosphatases. Total protein concentration was determined using the Bradford colorimetric assay by measuring absorbance at 595 nm with a Spark microplate reader (Tecan Group Ltd., Switzerland). Equal amounts of protein (30 μg per sample) were separated by Tris–glycine SDS–PAGE and transferred onto PVDF membranes (Immobilon-P; Millipore, Darmstadt, Germany) using a semi-dry transfer system (Biometra Fastblot; Analytik GmbH+Co, Jena, Germany). Membranes were incubated overnight at 4 °C with primary antibodies diluted in Tris-buffered saline (TBS) containing 0.1% (w/v) Tween-20 and 1% (w/v) bovine serum albumin. The primary antibodies used were: mouse anti-UCP1 (1:500, MAB6158, R&D Systems), mouse anti-LC3B (1:1000, sc-376404, Santa Cruz), rabbit anti-p62 (1:1000, P0067, Merck), and rabbit anti-HO-1 (1:1000, A11102, AB Clonal). Mouse β-actin antibody (1:1000, A2228, Sigma Merck, Darmstadt, Germany) and mouse anti-GAPDH antibody (1:1000, sc-47724, Santa Cruz) were used as loading controls. After incubation with the primary antibodies, membranes were washed in TBS containing 0.1% (w/v) Tween-20 and then incubated for 1 h at room temperature with horseradish peroxidase (HRP)-conjugated secondary

antibodies. The HRP-conjugated secondary antibodies used were goat anti-rabbit IgG (1:4000, Millipore) and goat anti-mouse IgG (H+L) (1:5000, A90–116P, Bethyl). Chemiluminescence detection of HRP-conjugated secondary antibodies was performed using a G:box chemi XX6/XX9 (Syngene, Cambridge, UK) and quantified using ImageJ 1.53r software.

2.10. Statistical analysis

For mitochondrial and lipid droplet analyses, quantitative parameters were calculated per image and images were treated as the analytical unit for statistical comparison. Fields of view were obtained from two independent differentiation experiments, which were considered as biological replicates, whereas images represent technical measurements within each replicate.

As the mitochondrial data were not normally distributed according to the Shapiro–Wilk test, the non-parametric Kruskal–Wallis test followed by Dunn's post hoc test for multiple comparisons was used (GraphPad Prism 9).

Principal component analysis (PCA) with Varimax rotation and Kaiser normalization was performed to integrate mitochondrial morphological parameters into a single multivariate model. The variables analysed included mitochondrial subtype ratios, mitochondrial number, mean area, mean perimeter, mean aspect ratio, mean form factor, branches per mitochondrion, total branch length per mitochondrion, mean branch length, branch junctions per mitochondrion, branch end points per mitochondrion, and mean branch diameter. This approach was used to maximise discrimination among differentiation time points and to identify the principal components contributing most to parameter separation. All these data were analysed using XLSTAT (Addinsoft, 2022).

The percentage of LDs area and median Feret diameter (µm) were analysed using the Kruskal–Wallis test followed by Dunn's post hoc test for multiple comparisons (GraphPad Prism 9).

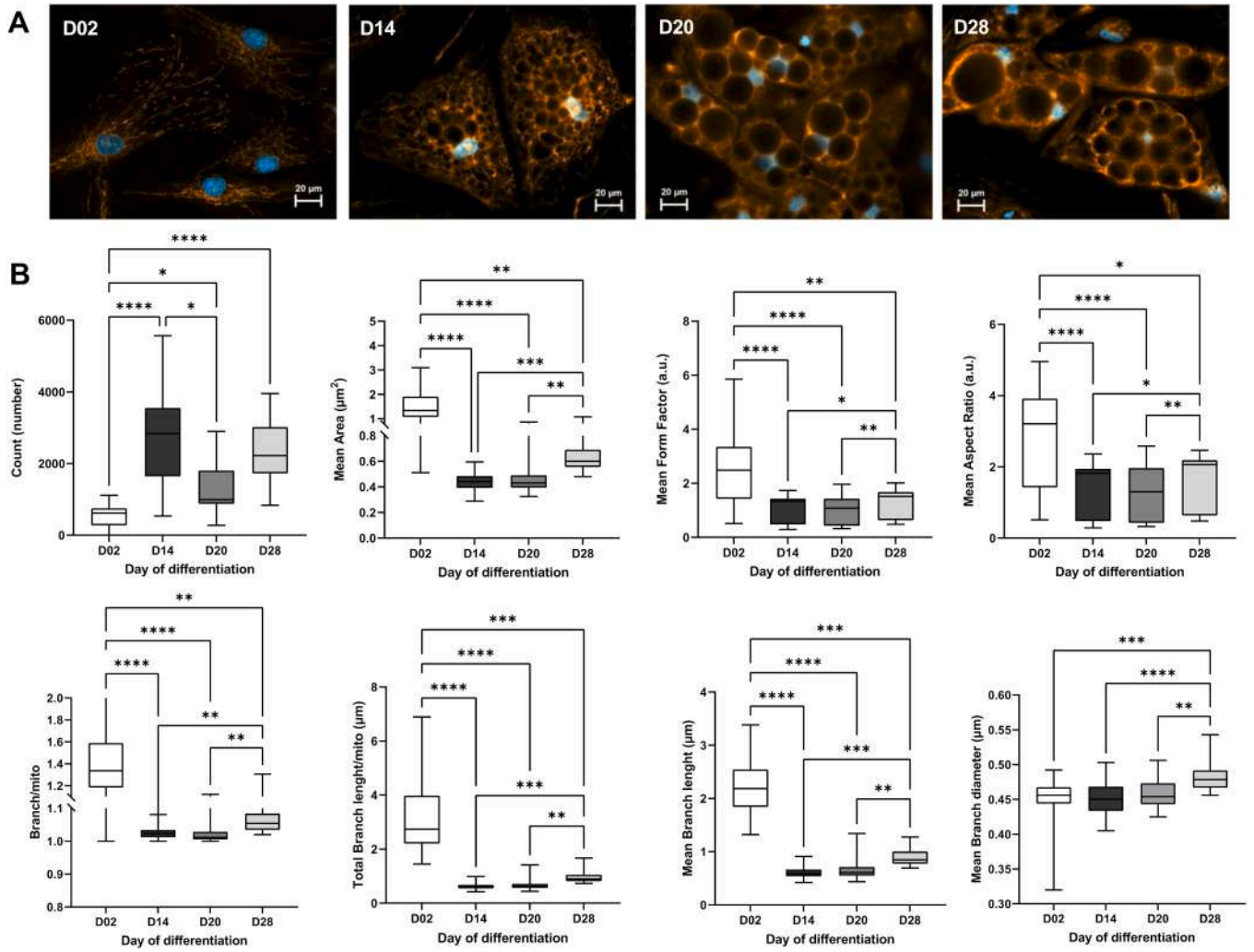

Fig. 1. Mitochondrial change during SGBS cell differentiation. A) Representative fluorescence images of SGBS cells stained with MitoTracker™ at different days of differentiation. Mitochondrial changes were quantified in over 131,000 mitochondria using the Mito Analyser and MicroP software. Scale bar: 20 µm. B) Mitochondrial analyses performed with the Mitochondrial Analyzer. Differences in the distribution of mitochondrial morphological features and in mitochondrial branching were analysed between cells at different days of differentiation. Count, number of mitochondria. Mitochondrial size was measured as average surface area. Shape was assessed using mean form factor and mean aspect ratio. Branch/mito indicates the number of branches per mitochondrion; total branch length/mito, the total length of branches per mitochondrion; mean branch length, the average length of branching; mean branch diameter, the average diameter of branching. Boxplots show medians (horizontal lines), first to third quartiles (box), and the most extreme values within the interquartile range (whiskers) across differentiation stages. Statistical significance was determined using the Kruskal–Wallis test. Quantitative analysis was performed at the image level. A minimum of 14 independent fields of view per differentiation day were analysed, obtained from two independent differentiation experiments. Each image contained between 2 and 6 cells depending on the day of differentiation. Morphological parameters were calculated per image and images were treated as the unit of analysis for statistical comparison. Cells at 2 days (D02), 14 days (D14), 20 days (D20), and 28 days (D28) of differentiation are depicted.

Protein expression ratios were determined from five technical measurements derived from the same differentiation experiment for each time point. Western blot quantifications are presented descriptively and were not subjected to inferential statistical testing.

RNA-seq differential expression was analysed separately using DESeq2 with FDR correction, as detailed in Section 2.6.

3. Results

3.1. Mitochondria morphology quantification

In adipocytes, mitochondria undergo considerable changes during differentiation. In SGBS cells, mitochondria are distributed in a reticular pattern at D02, become spherical around the lipid droplets at D14, and then switch to a tubular and interconnected form at D20 and D28 (Fig. 1**A**).

A comprehensive morphological analysis was performed on the mitochondria of SGBS cells at different stages of differentiation by measuring several parameters with the Mitochondrial Analyzer tool, as summarised in Fig. 1**B**. A significantly higher number of mitochondria was detected in differentiated cells at D14 and D28, whereas the mean mitochondrial area was significantly higher in cells at D02 compared to all other differentiation timepoints (Fig. 1**B**). In contrast, no statistical differences were observed between D14 and D20 cells for any of the parameters measured. Form factor and aspect ratio, commonly used as descriptors of mitochondrial shape, decreased significantly in cells at D14 and D20 compared to cells at D02 and D28 (Fig. 1**B**).

The Mitochondria Analyzer tool was also used to quantify the connectivity and morphological complexity of the mitochondrial network in differentiated SGBS cells. The total number and total length of branches per mitochondrion, as well as the mean branch length, were highest in D02 cells and showed significant differences compared to cells at other differentiation time points. In contrast, the mean branch diameter was significantly highest in D28 cells, but showed no differences between D02, D14, and D20 (Fig. 1**B**).

It should be noted that the Micro2P software can classify up to six morphological subtypes and calculate the average proportion of mitochondrial subtypes within each treatment. However, as the numbers of large globes, twisted tubes, and donuts were very low, only small globes, simple tubes, and branched tubes were included in the analyses.

The average proportion of mitochondria in the cells at different stages of differentiation was as follows: 8.51% in D02 cells, 66.13% in D14 cells, 14.80% in D20 cells, and 10.56% in D28 cells. Considering all timepoints of differentiation together, small globes (49.4%) and branched tubules (31.3%) were the most representative subtypes, followed by simple tubes (19.4%). While small globes were the most prevalent type in D14 cells (48.6%), simple tubes were predominant in D02 cells (41.3%). In contrast, the proportion of branched tubes increased over time (19.9% at D02, 30.8% at D14, 41.2% at D20, and 46.8% at D28) (Fig. 2). In detail, D28 cells showed 53% fewer small globes compared to D14 ($p < 0.0001$), but 58% and 34% more branched tubes compared to D02 and D14, respectively ($p < 0.0001$). D02 cells showed 61.6% and 51% more simple tubes compared to D14 and D28, respectively ($p < 0.0001$). The percentage area for the three mitochondrial subtypes was 18.5% for small globes, 20.96% for simple tubes, and 60.6% for branched tubes.

To assess the extent of differentiation days and the specific variation in an unbiased way, all the measurements obtained using the Mitochondrial Analyzer (i.e. number, mean area, mean perimeter, mean aspect ratio, mean form factor, branches/mito, total branch length/mito, mean branch length, branch junctions/mito, branch end points/mito, mean branch diameter) as well as the total number of mitochondria and the percentage of each mitochondrial subtype (i.e. small globe, simple tube, branching tube) calculated by the Micro2P software, were summarised in a single principal component analysis (PCA) (Fig. 3). Notably, each differentiation time point clustered in a distinct quadrant

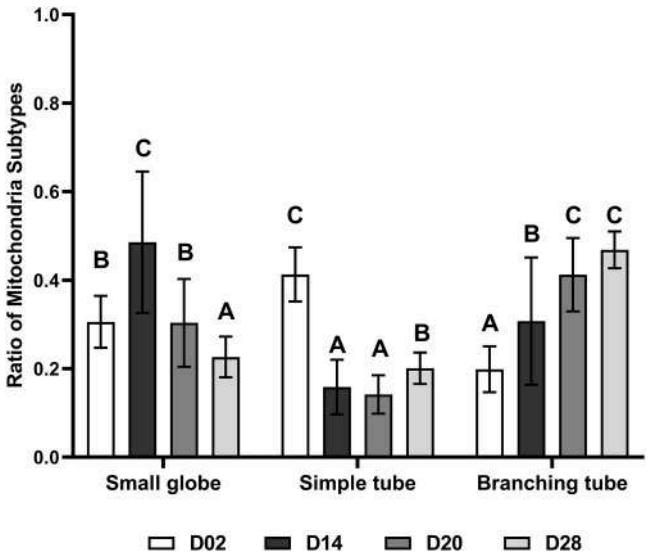

Fig. 2. Average ratio of mitochondrial subtypes in cells at different days of differentiation. Different superscript capital letters indicate significant differences ($p < 0.0001$). Differentiation on day 2 (D02), on day 14 (D14), on day 20 (D20) and on day 28 (D28). Quantification was performed at the image level from a minimum of 14 independent fields of view per differentiation stage, obtained from two independent differentiation experiments. Mitochondrial subtype proportions were calculated per image and used as the unit of analysis for statistical comparison.

of the PCA plot, providing further evidence that the mitochondrial measurements separated them into different and specific morphological phenotypes. The loading factors with the highest squared cosine values (cos^2) at F1 and F2 are the mean form factor, mean perimeter, mean area, and Branch End Points/mito; at F3, the percentage of small globes is the largest (Table 1).

PCA was used as an exploratory multivariate tool to integrate morphological parameters and is descriptive; it does not constitute inferential statistical testing. Its outcome depends on variable selection and scaling and should therefore be interpreted as pattern-based dimensional reduction rather than formal statistical evidence of group separation. Interpretation of PCA results should also be considered within the context of image-level analytical units derived from independent differentiation experiments.

3.2. Lipid droplet expansion and unilocular remodelling over time

Confocal microscopy analysis of SGBS cells stained with Bodipy™ at the differentiation stages considered showed that lipid content (i.e. the percentage of the imaged field area occupied by lipid droplets) increased markedly ($p < 0.001$) by D14 and remained elevated through D28 (Fig. 4**A**). In parallel, the field-level Feret median of droplet size approximately doubled from D02 to D14, then plateaued between D20 and D28 ($p < 0.001$) (Fig. 4**B**).

3.3. Mature adipocytes clustered together

To characterise transcriptional changes during the beige-to-white transition, the global organisation of the RNA-seq dataset was first assessed. After removing low-abundance reads, the final mapping rate of the filtered transcript reads was 59.0%. Initial analysis of the RNA-seq results included hierarchical clustering, which revealed differences between genes and showed that the transcriptome data were well clustered according to the day of differentiation. PCA revealed overall variability in the expression profiles of samples at different days of differentiation. In particular, the first principal component accounted for 73.8% of the variance and clearly differentiated D14, D20, and D28 from the early

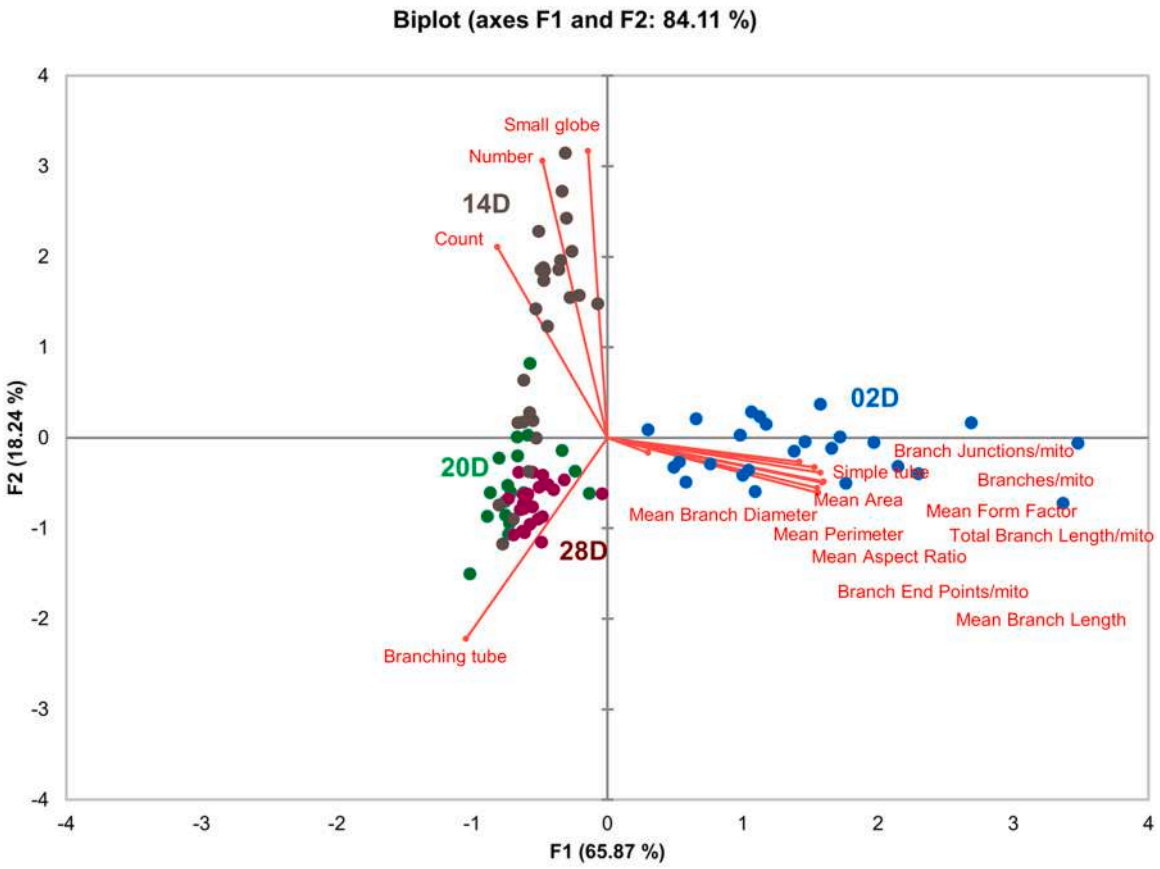

Fig. 3. Principal component analysis (PCA) biplot to visualise the information of the mitochondrial data set in differentiation days. The two-component model explained 84.1% of the variance in the data set and led to partial group separation. F1 and F2 are loading factors. D02, differentiation on day 2; D14, differentiation on day 14; D20, differentiation on day 20 and D28, differentiation on day 28.

Table 1
Squared cosines (cos^2) after Varimax rotation.

	F1	F2	F3
Mean Form Factor	**0.962**	**0.829**	0.002
Mean Perimeter	**0.959**	**0.889**	0.011
Total Branch Length/mito	**0.958**	0.006	0.016
Mean Area	**0.947**	**0.438**	0.000
Branch End Points/mito	**0.932**	**0.394**	0.012
Mean Branch Length	**0.914**	0.022	0.012
Mean Aspect Ratio	**0.904**	0.021	0.010
Branch Junctions/mito	**0.881**	0.027	0.000
Branches/mito	**0.880**	0.021	0.007
Simple tube	**0.757**	0.009	0.008
Branching tube	0.411	0.021	0.008
Count	0.249	0.033	0.006
Num Of Object	0.086	0.009	0.006
Mean Branch Diameter	0.034	0.013	0.016
Small globe	0.008	0.002	**0.944**

The table presents the squared cosine (cos^2) values, indicating the quality of representation of each mitochondrial variable to the rotated factors. Higher cos^2 values correspond to a stronger contribution of the variable to the corresponding principal component.

differentiation days D0 and D02, while the second component accounted for only 14.4% of the differences (Fig. 5**A**).

DEGs were analysed between D0, D02, D14 and D20 compared to D28, with a log_2fold change of |1.0| and an FDR-adjusted p-value of ≤ 0.05 (Table S1). iDEP2.1 expression analysis revealed a significant upregulation of 5064 genes in D28 compared to D0, 4375 in D28 compared to D02, 2577 in D28 compared to D14 and 534 in D28 compared to D20. In addition, significant downregulation of 4816 genes was detected in D28 *vs* D0, 4105 in D28 *vs* D02, 2715 in D28 *vs* D14 and 751 in D28 *vs* D20.

A total of 127 and 60 common DEGs were consistently upregulated and downregulated, respectively, in the overlapping regions of the Venn diagrams (Fig. 5**B, C**). In addition, a different number of genes showed unique expression patterns for each of the four differentiated days compared to day 28. Specifically, 1348 genes were upregulated at D0, 851 at D02, 705 at D14 and 107 at D20 (Fig. 5**B**), while 1591 genes were downregulated at D0, 997 at D02, 835 at D14 and 224 at D20 (Fig. 5**C**). The number of upregulated and downregulated DEGs decreased from D28_D0 to D28_D20. The largest number of induced or repressed transcripts was observed at D28_D0.

3.4. Integrated GO and KEGG enrichment analysis reveals a reverse mitochondrial signature and upregulation of HIF-1, autophagy and FoxO signalling at D28 compared to D14

Functional enrichment analysis identified significant alterations in pathways associated with mitochondrial metabolism, lipid catabolism and extracellular matrix organisation. Full Gene Ontology (BP, CC and MF) enrichment results are provided in Tables S2–S4. Among the differentially regulated BP, 'Anatomical structure morphogenesis' was downregulated in the comparisons D28 *vs* D0 and D28 *vs* D02 but instead resulted upregulated in D28 *vs* D14 and in D28 *vs* D20. In the D28 *vs* D0 and D28 *vs* D02 comparisons, the upregulated genes were involved in the 'Fatty acid metabolic process', the 'Lipid metabolic process' and the 'Organic acid metabolic process', while these BPs were downregulated in the D28 *vs* D20 comparison. In contrast, DEGs involved in 'Cell adhesion' were downregulated in the comparisons D28 *vs* D0 and D28 *vs* D02, whereas were upregulated in the comparison D28 *vs* D20. Upregulated

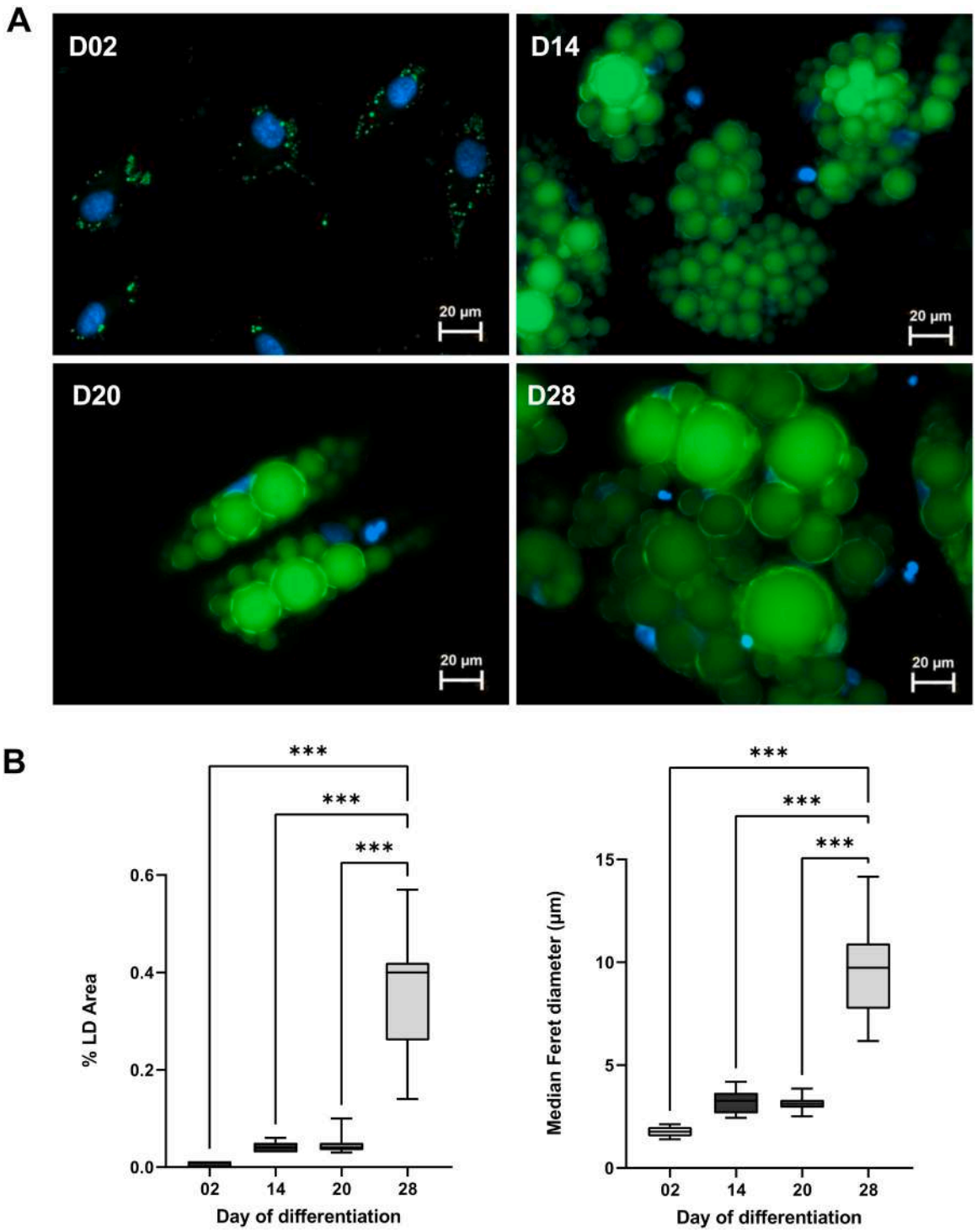

Fig. 4. Lipid droplet expansion and unilocular remodelling during differentiation. A) Representative fluorescence images of SGBS cells stained with Bodipy™ at different days of differentiation. Nuclei were counterstained with Hoechst. Scale bar: 20 µm. B) Quantitative analysis of lipid droplet remodelling during differentiation. Boxplots show medians (horizontal lines), first to third quartiles (box), and the most extreme values within the interquartile range (whiskers) across the differentiation days. Statistical significance in the boxplots was determined by the Kruskal-Wallis test. Quantification was performed at the image level. At least seven independent fields of view per time point were analysed, obtained from two independent differentiation experiments. Each box represents an independent field of view (one data point = one image). LD parameters were calculated per image and used as the unit of analysis for statistical comparison. The percentage of LD area and the median Feret diameter increased markedly at D28. Differentiation was assessed on day 2 (D02), day 14 (D14), day 20 (D20), and day 28 (D28).

DEGs in D28 compared to D14 were enriched in 'Developmental process' and in 'Cell differentiation' (Fig. 6**A**). Interestingly, down-regulated DEGs enriched in 'Cellular respiration', 'Mitochondrial gene expression', 'Energy derivation by oxidation of organic compounds', 'Oxidative phosphorylation' and 'Respiratory electron transport chain' were only reported in D28 compared to D14 (Fig. 6**A**).

Among the CC-enriched pathways, upregulated DEGs associated with 'Mitochondrion', 'Mitochondrial membrane' and 'Mitochondrial matrix' were enriched in D28_D0 and D28_D02 comparisons, but the same CCs were downregulated in D28_D14 and D28_D20 comparisons

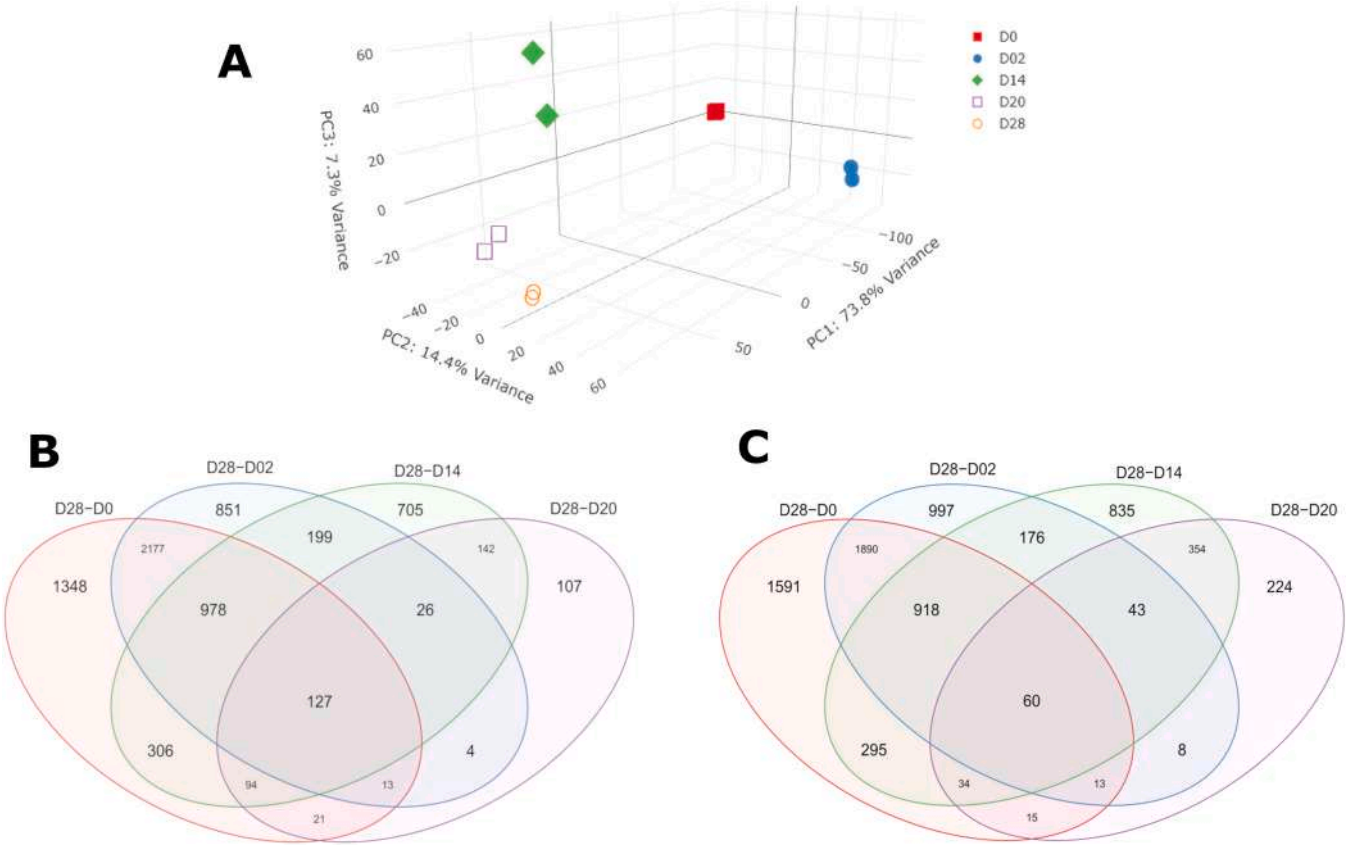

Fig. 5. PCA and Venn diagrams with upregulated and downregulated DEGs, A) Principal component analysis (PCA) was applied to SGBS samples collected at different stages of differentiation. The analysis confirmed the high quality of the transcriptomic data, as biological replicates clustered consistently according to differentiation stage. Early-stage samples (D0 and D02) were clearly separated from later stages (D14, D20, and D28) along the first principal component, while separation between D0 and D02 was observed along the second component. B) Upregulated DEGs on each day of differentiation compared to D28. C) Downregulated DEGs on each day of differentiation compared to D28. Significant DEGs were defined as those with $p < 0.05$ and a $\log_2$ fold change greater than 1 or less than - 1. The results show that 127 and 60 overlapping transcripts were consistently upregulated and downregulated, respectively, in the comparisons.

(Fig. 6**B**). Upregulated DEGs in the D28_D0 and D28_D02 comparisons were also enriched in the 'Oxidoreductase complex', but the 'Respiratory chain complex' was only enriched in D28_D02 comparison. DEGs involved in 'Extracellular space' and Extracellular region' were downregulated in D28_D0 and D28_D02, but those in 'Extracellular matrix' and Extracellular region' were upregulated in D28_D14 and D28_D20 (Fig. 6**B**). 'Anchoring junction', 'Cell-substrate junction' and 'Focal adhesion' were only downregulated in D28_D0 comparisons (Fig. 6**B**). Downregulated DEGs involved in pathways related to 'Ribosome' were only specifically enriched in the D28_D14 comparison (Fig. 6**B**).

'Oxidoreductase activity' and 'Electron transfer activity' were observed among the upregulated MFs in the D28_D0 and D28_D02 comparisons. In contrast, 'Oxidoreductase activity' was downregulated in the D28_D14 and D28_D20 comparisons. 'Actin binding' and Extracellular matrix structural constituent were downregulated in D28 compared to D0 and in D28 compared to D02 but upregulated in D28 compared to D14 and D28 compared to D20 (Fig. 6**C**). Downregulated DEGs enriched with 'Structural constituent of ribosome' were found in the D28_D0, D28_D02 and D28_D14 comparisons, while 'Rrna binding' was only downregulated in the D28_D14 comparison (Fig. 6**C**).

The scatter plot in Fig. 6**D** shows the results of the KEGG analysis and illustrates the enrichment of several signalling pathways identified at 28 days of differentiation compared with the other differentiation time points. It is noteworthy that the upregulated DEGs were mainly enriched in 'Metabolic pathways' 'Oxidative phosphorylation', 'PPAR signalling pathway' and 'Valine leucine and isoleucine degradation' compared to D28_D0 and D28_D02. In comparison to D28_D02 'Citrate cycle (TCA cycle) 'and, in D28_D02, 'Thermogenesis' were also upregulated. In contrast, 'Oxidative phosphorylation', 'Thermogenesis', 'PPAR signalling pathway' and 'Valine leucine and isoleucine degradation' were downregulated in the D28 *vs* D14 comparison. Interestingly, the signalling pathways 'Ferroptosis', 'HIF-1′, 'Autophagy' and 'AMPK signalling pathway' were significantly upregulated at D28 in comparison to D14. 'Focal adhesion' was upregulated in D28 in comparison to D20 (Fig. 6**D**). KEGG pathway enrichment, are reported in Table S5.

3.5. *Selection and analysis of hub genes in D28 vs D14 comparison*

Since the most pronounced transcriptional differences were observed between D28 and D14, the 705 uniquely up-regulated and 835 uniquely down-regulated DEGs from this comparison were used to construct protein–protein interaction (PPI) networks (interaction score > 0.4).

The down-regulated network comprised 672 nodes and 3663 edges, whereas the up-regulated network contained 647 nodes and 1731 edges. Using the MCODE plugin in Cytoscape, three highly connected clusters were identified among the down-regulated DEGs (MCODE scores: 27.673, 8.710, and 7.000; Fig. 7**A–C**) and three among the up-regulated DEGs (MCODE scores: 6.056, 5.667, and 5.091; Fig. 7**D**).

Key hub nodes within each cluster were identified using CytoHubba, applying the Maximal Clique Centrality (MCC) algorithm.

In the first down-regulated cluster, the top ten hub genes were MRPL21, MRPL36, MRPS12, MRPL1, MRPS15, MRPS14, MRPL24, MRPS18C, MTIF2, and MRPL32, all involved in mitochondrial translation elongation/termination (Fig. 7**E**).

In the second down-regulated cluster, the top ten hub genes (ETFB, ACADSB, CPT2, ACCA1, EHHADH, ACAD8, ETFDH, ECH1, SCP2, and

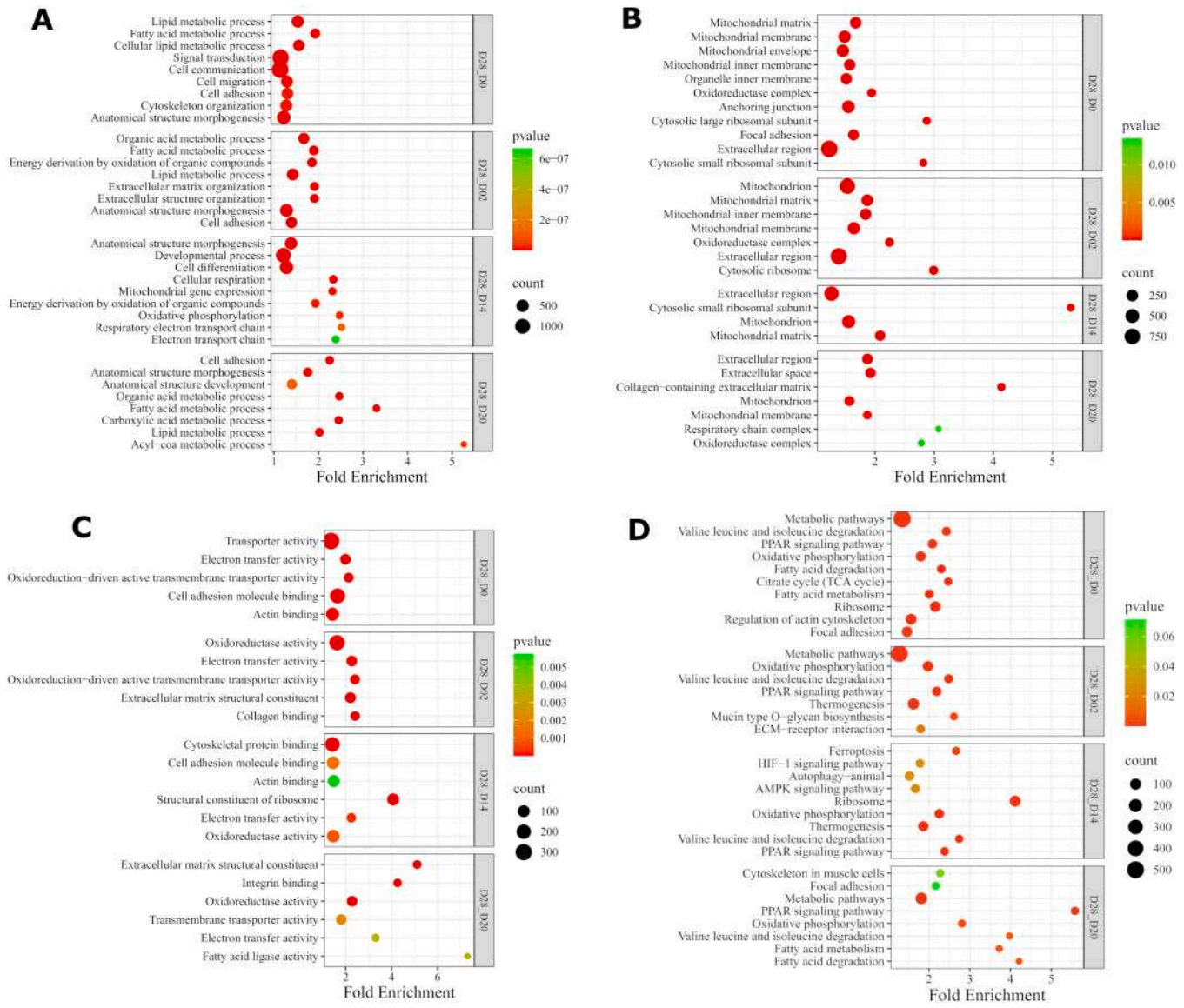

Fig. 6. GO and KEGG enrichment analysis at D28 compared to other differentiation days. Dot size represents the number of genes in each pathway. The colours of the dots are arranged in order of significance, with red being the most significant, followed by orange and green. A) Biological processes. B) Cellular components. C) Molecular functions. D) KEGG pathways. Figure was plotted by http://www.bioinformatics.com.cn/srplot.

HSDL2) were enriched in pathways related to fatty-acid metabolism, branched-chain-amino-acid degradation, β-oxidation, PPAR signalling, thermogenesis, and the mitochondrial compartment (Fig. 7**F**).

The third cluster comprised seven DEGs associated with the citrate (TCA) cycle and the mitochondrial tricarboxylic-acid-cycle enzyme complex.

Conversely, in the up-regulated network, CytoHubba identified BECN1, WIPI1, MAP1LC3A, NBR1, ULK1, LAMP2, USP39, CYFIP1, PAK4, and SART1 as the top ten hub genes (Fig. 7**G**), all functionally enriched in autophagy-related pathways and the autophagosome compartment.

The remaining up-regulated clusters were not analysed further because of low connectivity and MCC scores only slightly above 5, which precluded reliable hub-gene prioritisation.

Representative enriched terms for each MCODE cluster are reported in Table S6, and full enrichment results are provided in Table S7.

These results were also confirmed by parametric gene set enrichment analysis (PGSEA), which treated the principal component loadings as expression levels and showed significantly higher expression of 'Autophagy', 'HIF-1 signalling pathway' and 'Mitophagy', while the 'PPARG signalling pathway" was downregulated (Fig. 8).

3.6. Differentiated SGBS cells acquire BAT phenotype

Based on RNA-seq data from cells at each differentiation day, the BATLAS tool was used to estimate the relative contribution of BAT and WAT gene signatures from normalised read counts. The analysis indicated the lowest predicted BAT signature at D0 and D02, with a reduction at D28 compared to D14, which was consistently observed across biological replicates. In contrast, the predicted WAT signature was reduced compared with early differentiation days and increased again at D28 (Fig. 9).

3.7. Downregulation of thermogenic markers and activation of autophagy at late differentiation stage

To characterise the molecular remodelling accompanying the transition from the transient brown-like state to late-stage whitening, RNA-seq data and bioinformatic analysis were used to examine the expression of key thermogenic and stress-related protein markers during

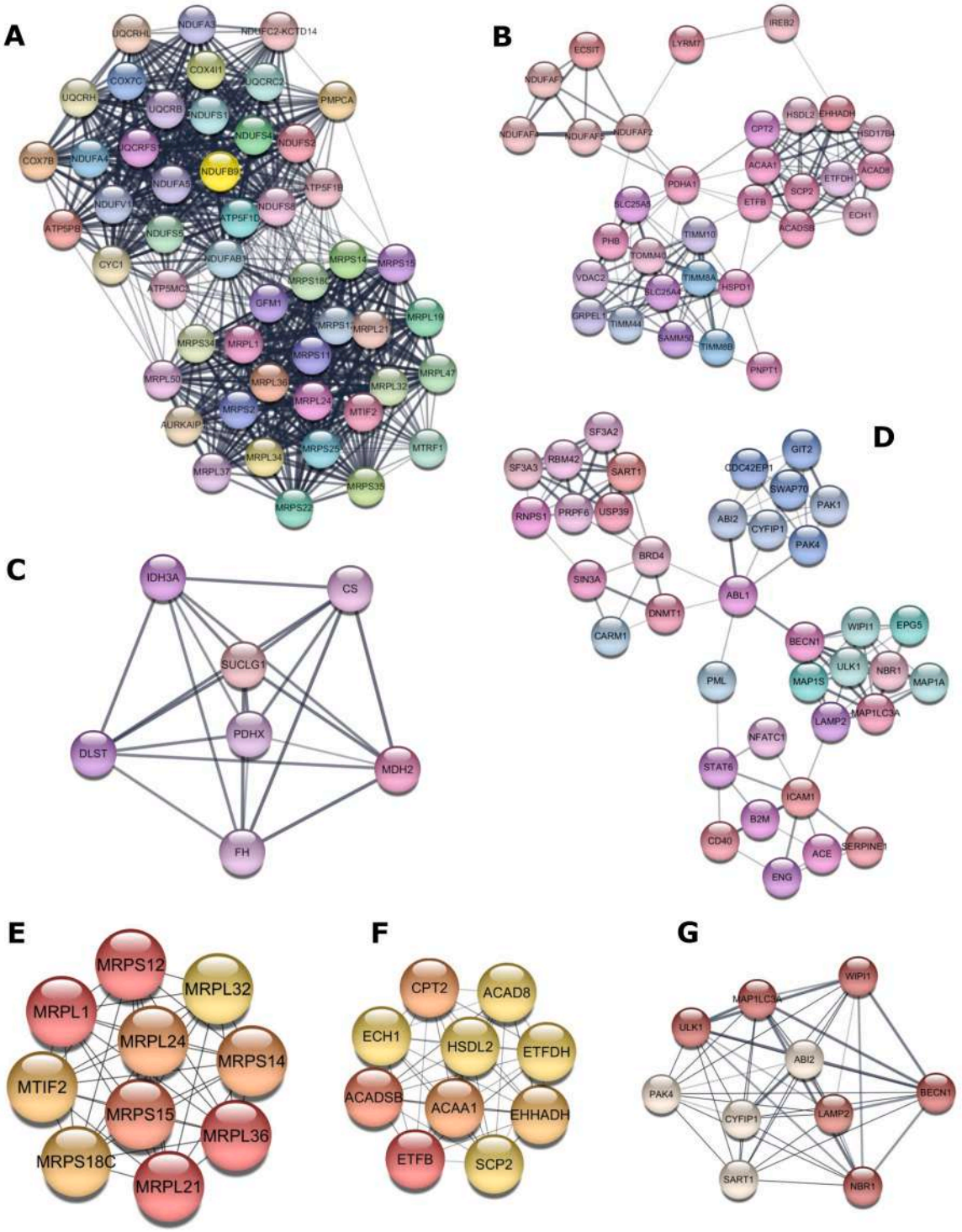

Fig. 7. Key clusters of PPI networks identified by MCODE analysis and their associated downregulated (A, B, C) and upregulated (D) hub genes in the D28_D14 comparison. A) Cluster 1 (score 27.673); B) Cluster 2 (score 8.710); C) Cluster 3 (score 7.0); D) Cluster 1 (score 6.056). E) Top 10 downregulated hub genes from cluster 1; F) Top 10 downregulated hub genes from cluster 2; G) Top 10 upregulated hub genes from cluster 1.

differentiation. The selected protein markers were chosen to represent key biological modules identified by transcriptomic and network analyses, including thermogenic identity (UCP1), the browning-associated oxidative phase (HO-1), and autophagy-related remodelling (p62/SQSTM1 and LC3B). As expected, UCP1 protein expression peaked strongly at day 14 and declined markedly by day 28, confirming the loss of thermogenic identity (Fig. 10**A, B**). Concurrently, HO-1 (HMOX1), which is typically induced during the early oxidative and pro-thermogenic phase, decreased from D14, indicating resolution of the browning-associated redox response and a shift toward a metabolically more quiescent state (Fig. 10**A, C**). In contrast, autophagy markers showed a distinct activation profile: p62/SQSTM1 levels were reduced, while LC3B-II remained detectable despite a lower LC3B-II/LC3B-I ratio at 28 days of differentiation, a pattern consistent with enhanced autophagic flux rather than impaired autophagy (Fig. 10**D, E, F**). Together, these molecular changes support a model in which whitening is

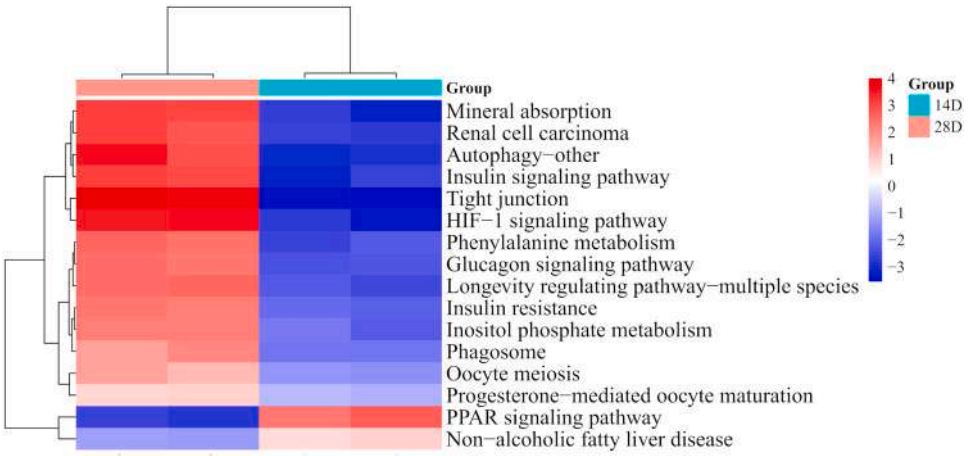

Fig. 8. PGSEA using KEGG showed the pathways activities in D14 and D28.

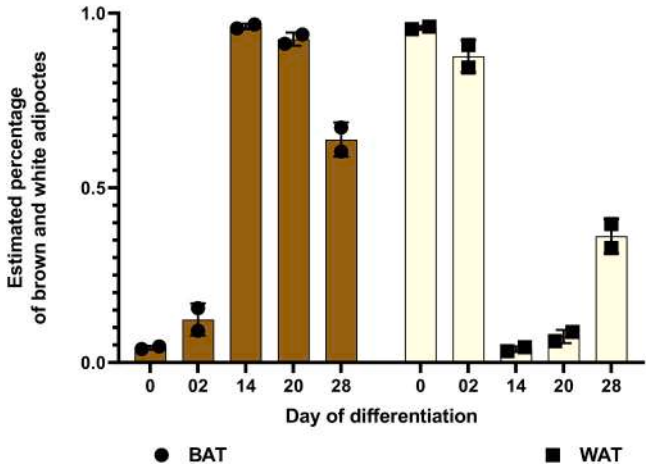

Fig. 9. BATLAS-derived transcriptomic prediction of brown (BAT) and white (WAT) adipocyte signatures across differentiation. Data represent n = 2 independent RNA-seq biological replicates per condition. Each dot corresponds to one independent transcriptomic sample; bars indicate mean ± SD. Results should be interpreted as transcriptomic trends given the limited number of biological replicates.

accompanied by suppression of thermogenic and oxidative-stress programmes and activation of autophagy-dependent mitochondrial remodelling.

4. Discussion

SGBS cells provide a useful *in vitro* model to explore key aspects of human adipocyte biology and their role in metabolic diseases. SGBS cells have been extensively characterised at the molecular level (Tews et al., 2022), and it is well established that they undergo functional browning during differentiation, predominantly driven by rosiglitazone-mediated activation of PPARγ (Halbgebauer et al., 2020; Klusóczki et al., 2019). Previous transcriptomic analyses have shown that genes upregulated during the early browning phase (days 4–10) are mainly associated with extracellular matrix remodelling and oxidative stress, both known regulators of thermogenesis (Colitti et al., 2022). This transient activation is consistent with *in vivo* observations showing that beige/brown characteristics are rapidly reversible under reduced thermogenic demand (Jun et al., 2017; Shimizu et al., 2014).

In this study, the decline of the transient brown phenotype was examined by comparing gene expression profiles at days 0, 2, 14, and 20 with those at day 28 of differentiation. BATLAS-based transcriptomic prediction indicated a reduced predicted thermogenic signature at D28 compared to D14, a trend consistently observed across both independent RNA-seq replicates. However, the limited number of biological replicates warrants cautious interpretation.

Consistent with previous observations that early differentiation stages are characterised by the induction of extracellular matrix- and oxidative stress–related genes associated with beige identity (Colitti et al., 2022), HO-1 protein levels did not increase at day 14, which coincided with the peak of UCP1 expression. This supports a temporal separation between early stress-responsive programmes and the establishment of the thermogenic phenotype. In this context, the selected protein markers were intended to validate downstream phenotypic and autophagy-related transitions identified at the transcriptomic level, rather than to establish upstream signalling hierarchy.

Notably, the reduction in thermogenic features at day 28 did not represent a passive decline; rather, the data indicated an actively regulated metabolic transition. Here, whitening refers to the late differentiation stage (D28) following peak browning (D14) and is defined not as a passive loss of browning features, but as an adaptive metabolic remodelling state characterised by coordinated suppression of thermogenic and oxidative programmes, along with structural and signalling reorganisation of mitochondrial function. By 28 days of differentiation, a coordinated downregulation of oxidative and PPARγ-dependent programmes was accompanied by enrichment of HIF-1, FoxO, and AMPK-related signalling pathways, along with autophagy–mitophagy-associated modules (Altshuler-Keylin et al., 2016; Kang et al., 2024; Lu et al., 2018). This pattern is consistent with a transition to a metabolically less oxidative and more maintenance-oriented state, rather than a simple loss of differentiation potential. While these observations suggest coordinated pathway engagement, they are based on associative transcriptomic and protein-level evidence and do not establish a direct mechanistic hierarchy. This adaptive reorientation supports cellular survival under reduced thermogenic demand and corresponds to the reversible nature of browning observed in vivo, where oxygen availability and nutrient flux tightly regulate adipocyte phenotypes (Lee and Cowan, 2013; Shimizu et al., 2014).

Indeed, the morphological quantification of SGBS cells supports this functional interpretation. Through coordinated fission and fusion, mitochondria maintain their structural organisation and cellular distribution. In adipocytes, this dynamic regulation produces a continuum of mitochondrial morphologies, ranging from highly interconnected networks to discrete fragments, consistent with observations in SGBS cells (Montanari and Colitti, 2018). Although the number of mitochondria remains elevated at D28, the network adopts a thicker, more stabilised architecture rather than the highly dynamic, fragmented morphology typical of cells at D14. Thus, cells at D14 and D28 possess a greater

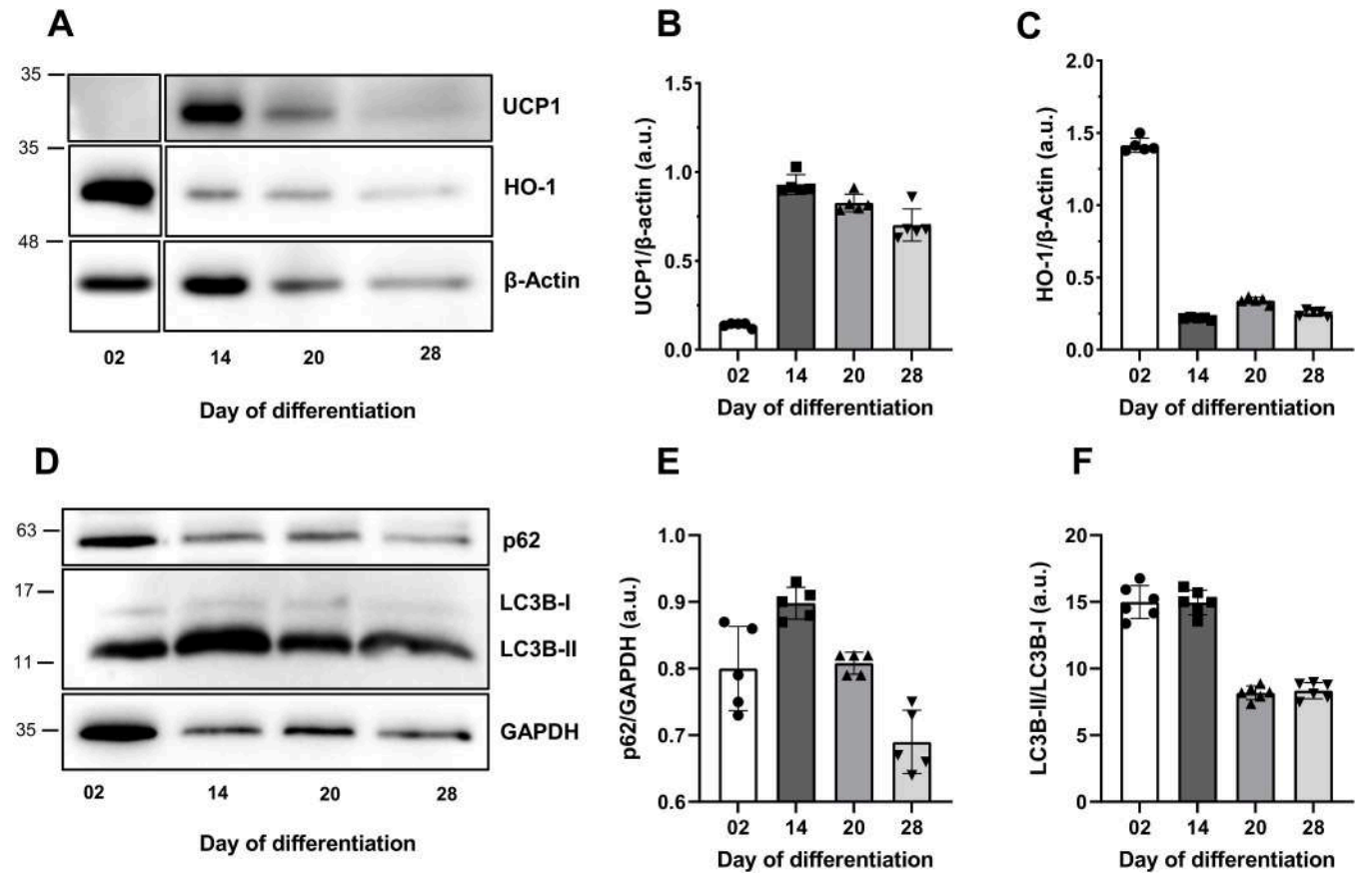

Fig. 10. Expression of thermogenic, oxidative-phase, and autophagy-related markers during SGBS adipocyte differentiation. (A) Representative Western blots showing UCP1, HO-1, and β-Actin at days of differentiation (D02, D14, D20, D28). Two non-adjacent regions of the same blot and same acquisition were merged as indicated by the double line. (B) Densitometric quantification of UCP1/ β-Actin confirms maximal expression at D14 and a marked decline at D28. (C) Quantification of HO-1/ β-Actin shows a marked reduction at D28 compared with D02, indicating attenuation of the browning-associated oxidative response. (D) Representative Western blots showing p62/SQSTM1, LC3B-I/LC3B-II, and GAPDH at different days of differentiation (D02, D14, D20, D28). (E) Quantification of p62/GAPDH showing reduced level at D28, consistent with enhanced autophagic flux rather than autophagy blockade. (F) Quantification of the LC3B-II/LC3B-I ratio showing a clear decrease at D28 consistent with accelerated LC3B-II turnover during enhanced autophagic flux. Data represent five technical measurements derived from the same differentiation experiment. Each dot corresponds to a single technical measurement; bars indicate the mean ± SD. Western blot quantifications are presented descriptively as supportive validation consistent with the transcriptomic findings.

number of mitochondria, whereas D02 cells have a smaller average mitochondrial area and the most complex network organisation. D14 and D20 cells exhibit similar characteristics, with a reduced form factor and aspect ratio compared to either D02 or D28 cells, while at D28, cells show the highest mean branch diameter. Notably, transcriptomic analysis is entirely consistent with these observations of mitochondrial morphology. Hub gene analysis at D28 identified core autophagy regulators (BECN1, ULK1, LC3 family members) among the most central nodes, indicating active mitochondrial clearance rather than simple mitochondrial degeneration (Altshuler-Keylin et al., 2016). Interestingly, the overall signature aligns with a functional shift from energy dissipation to cellular preservation. Future studies directly assessing mitochondrial bioenergetic function would help determine how the observed structural remodelling translates into functional oxidative capacity during late-stage adipocyte whitening.

Lipid droplet remodelling further supports this metabolic reorientation. LD morphology and its interaction with mitochondria are actively remodelled during browning in mouse adipocytes (Cui et al., 2019; Yu et al., 2015). By D28, SGBS adipocytes showed marked unilocular remodelling, characterised by increased LD surface area and stabilised droplet architecture, consistent with a shift towards lipid storage rather than oxidation. These structural changes parallel the suppression of oxidative gene programmes and the activation of autophagy-mediated recycling, indicating a coordinated reorganisation of mitochondrial-lipid droplet crosstalk during whitening.

At the molecular level, the transcriptomic signature observed at D28, characterised by downregulation of PPAR signalling, oxidative phosphorylation, and thermogenic pathways, along with upregulation of AMPK, HIF-1, ferroptosis, and autophagy-related pathways, strongly suggests functional metabolic rewiring away from a brown/oxidative phenotype. Although these transcriptomic patterns were identified using FDR-controlled differential expression analysis, the limited number of biological replicates warrants cautious interpretation of pathway-level conclusions. Additionally, modulation of selected ferroptosis-related genes was observed: GPX4, SLC7A11, ACSL4, and ALOX15B were downregulated at D28 compared to D14, whereas FTH1 was upregulated. This pattern is consistent with remodelling of iron and lipid redox homeostasis – a compensatory stress-adaptive response – rather than induction of overt ferroptotic cell death. Notably, the RNA-seq profile and bioinformatic analysis are consistent with the Western blot data, which show decreased p62 levels and a reduced LC3B-II/LC3B-I ratio at D28. The combined behaviour of LC3B and p62 is consistent with increased autophagic flux during the whitening phase in SGBS differentiation. It should be noted that, although the level of LC3B-II decreases relative to that of LC3B-I, this does not indicate impaired autophagy. In fact, LC3B-II is rapidly degraded in autolysosomes when flux is high and therefore does not accumulate under conditions of accelerated turnover (Klionsky et al., 2016; Mizushima and Yoshimori,

2007). Consistently, the marked reduction of p62/SQSTM1 at D28 is compatible with increased cargo degradation, as p62 is selectively consumed during active autophagy (Klionsky et al., 2016, 2012). Overall, these molecular signatures suggest engagement of autophagy- and mitophagy-related processes during whitening, rather than inhibition of autophagy. Although these patterns are consistent with enhanced autophagic activity, direct flux measurements using lysosomal inhibition were not performed; therefore, autophagy activation should be interpreted as inferred rather than directly demonstrated. Together, these findings indicate that whitening is an actively regulated remodelling programme, not a passive regression of the thermogenic phenotype. HIF-1 signalling was identified in pathway enrichment analyses and supported by differential regulation of canonical hypoxia-responsive genes, including upregulation of SLC2A1 and HMOX1, during late-stage adipocyte whitening. This coordinated response is characterised by activation of the AMPK–HIF-1 axis and autophagy-driven mitochondrial reorganisation (Altshuler-Keylin et al., 2016; Lu et al., 2018). Rather than indicating terminal exhaustion, the D28 phenotype reflects a late-stage shift towards a less oxidative, more maintenance-oriented metabolic state driven by AMPK–HIF-1 signalling and increased autophagic activity. This framework is consistent with the reversible nature of browning observed in vivo and highlights mitochondrial quality control and lipid–organelle communication as central determinants of adipocyte plasticity. Future research should determine whether targeted modulation of these pathways can stabilise or re-induce thermogenic competence, thereby opening new avenues for metabolic intervention in obesity and related disorders (Speakman, 2025; Wang et al., 2025).

The coordinated activation of AMPK, HIF-1, and autophagy observed in late-stage SGBS adipocytes suggests that these pathways form a conserved adaptive module regulating energy efficiency and mitochondrial quality control. As AMPK activation promotes lipid oxidation and increases mitochondrial turnover, while HIF-1 and autophagy modulate cellular responses to hypoxia and metabolic stress, the interplay among these mechanisms may serve as a molecular switch controlling adipocyte fate.

Although extrapolation to in vivo adipose tissue requires further validation, the coordinated engagement of AMPK–HIF–autophagy-related pathways observed here may be relevant for metabolic regulation. From a translational perspective, this triad provides a conceptual framework for understanding mechanisms that could contribute to metabolic flexibility in obesity, a condition characterised by chronic nutrient overload, hypoxia, and impaired autophagic clearance. Pharmacological or nutritional modulation of this axis warrants investigation in appropriate in vivo and functional models, as its potential to influence adipocyte plasticity and metabolic balance remains to be directly demonstrated. In this context, our findings highlight the AMPK–HIF–autophagy signalling network as a biomarker framework of adipocyte phenotypic transitions rather than as a validated therapeutic target for reprogramming adipose tissue function. Elucidating how these pathways interact with nutrient- and oxygen-sensing mechanisms in vivo could provide a conceptual basis for future studies exploring metabolic interventions in obesity and related disorders.

5. Conclusion

In summary, this study demonstrates that whitening of SGBS adipocytes at late differentiation is not a passive regression, but a regulated metabolic adaptation. The coordinated suppression of thermogenic and oxidative programmes, together with activation of hypoxia-, AMPK-, and autophagy-associated pathways, indicates a shift towards a less oxidative and more maintenance-oriented white adipocyte-like phenotype. Morphological, transcriptomic, and lipid droplet analyses reveal a controlled reorganisation of mitochondrial function and lipid handling, rather than functional exhaustion.

These findings highlight the coordinated engagement of the AMPK–HIF–autophagy signalling network during late-stage whitening and provide a conceptual framework for understanding adipocyte phenotypic plasticity, rather than establishing a validated mechanistic hierarchy. Modulation of this axis requires further investigation in appropriate in vivo and functional models to determine its relevance for metabolic regulation in obesity and related disorders.

Funding and Support

This research— did not receive any specific grant from funding agencies in the public, commercial, or not-for profit sectors.

Author statement

We want to declare that the work described is original research that has not been published previously and is not under consideration for publication elsewhere. All the authors listed wish to be considered for publication in Tissue and Cell. No conflict of interest exists in submitting this manuscript; all authors have approved the paper for publication.

Authors' contributions

Giulia Polacchini: Writing – review & editing, Methodology, Investigation. **MONICA COLITTI:** Writing – review & editing, Writing – original draft, Investigation, Formal analysis, Data curation, Conceptualization. **Andrea Venerando:** Writing – review & editing, Methodology.

Declaration of Competing Interests

The authors declare that they have no known competing financial interests or personal relationships that could have appeared to influence the work reported in this paper.

Acknowledgements

We thank Prof. Martin Wabitsch (Division of Pediatric Endocrinology, Department of Pediatrics and Adolescent Medicine, University of Ulm, Ulm, Germany) for providing the SGBS cells.

Appendix A. Supporting information

Supplementary data associated with this article can be found in the online version at doi:10.1016/j.tice.2026.103482.

Data availability

Data will be made available on request.

References

Addinsoft. 2022. XLSTAT statistical and data analysis solution. USA: New York. Available at: ⟨https://www.xlstat.com/en⟩.

Altshuler-Keylin, S., Shinoda, K., Hasegawa, Y., Ikeda, K., Hong, H., Kang, Q., Yang, Y., Perera, R.M., Debnath, J., Kajimura, S., 2016. Beige Adipocyte Maintenance Is Regulated by Autophagy-Induced Mitochondrial Clearance. Cell Metab. 24, 402–419. https://doi.org/10.1016/j.cmet.2016.08.002.

Ashburner, M., Ball, C.A., Blake, J.A., Botstein, D., Butler, H., Cherry, J.M., Davis, A.P., Dolinski, K., Dwight, S.S., Eppig, J.T., Harris, M.A., Hill, D.P., Issel-Tarver, L., Kasarskis, A., Lewis, S., Matese, J.C., Richardson, J.E., Ringwald, M., Rubin, G.M., Sherlock, G., 2000. Gene ontology: tool for the unification of biology. Gene Ontol. Consort. Nat. Genet 25, 25–29. https://doi.org/10.1038/75556.

Cannon, B., Nedergaard, J., 2017. What Ignites UCP1? Cell Metab. 26, 697–698. https://doi.org/10.1016/j.cmet.2017.10.012.

Chaudhry, A., Shi, R., Luciani, D.S., 2020. A pipeline for multidimensional confocal analysis of mitochondrial morphology, function, and dynamics in pancreatic β-cells. Am. J. Physiol. Endocrinol. Metab. 318, E87–E101. https://doi.org/10.1152/ajpendo.00457.2019.

Chin, C.-H., Chen, S.-H., Wu, H.-H., Ho, C.-W., Ko, M.-T., Lin, C.-Y., 2014. cytoHubba: identifying hub objects and sub-networks from complex interactome. BMC Syst. Biol. 8 (4), S11. https://doi.org/10.1186/1752-0509-8-S4-S11.

Colitti, M., Ali, U., Wabitsch, M., Tews, D., 2022. Transcriptomic analysis of Simpson Golabi Behmel syndrome cells during differentiation exhibit BAT-like function. Tissue Cell 77, 101822. https://doi.org/10.1016/j.tice.2022.101822.

Cui, L., Mirza, A.H., Zhang, S., Liang, B., Liu, P., 2019. Lipid droplets and mitochondria are anchored during brown adipocyte differentiation. Protein Cell 10, 921–926. https://doi.org/10.1007/s13238-019-00661-1.

Cypess, A.M., Lehman, S., Williams, G., Tal, I., Rodman, D., Goldfine, A.B., Kuo, F.C., Palmer, E.L., Tseng, Y.-H., Doria, A., Kolodny, G.M., Kahn, C.R., 2009. Identification and importance of brown adipose tissue in adult humans. N. Engl. J. Med 360, 1509–1517. https://doi.org/10.1056/NEJMoa0810780.

Farmer, S.R., 2006. Transcriptional control of adipocyte formation. Cell Metab. 4, 263–273. https://doi.org/10.1016/j.cmet.2006.07.001.

Ge, S.X., Son, E.W., Yao, R., 2018. iDEP: an integrated web application for differential expression and pathway analysis of RNA-Seq data. BMC Bioinforma. 19, 534. https://doi.org/10.1186/s12859-018-2486-6.

Ge, X., 2021. iDEP Web Application for RNA-Seq Data Analysis. Methods Mol. Biol. 2284, 417–443. https://doi.org/10.1007/978-1-0716-1307-8_22.

Halbgebauer, D., Dahlhaus, M., Wabitsch, M., Fischer-Posovszky, P., Tews, D., 2020. Browning capabilities of human primary adipose-derived stromal cells compared to SGBS cells. Sci. Rep. 10, 9632. https://doi.org/10.1038/s41598-020-64369-7.

Jun, J.C., Devera, R., Unnikrishnan, D., Shin, M.-K., Bevans-Fonti, S., Yao, Q., Rathore, A., Younas, H., Halberg, N., Scherer, P.E., Polotsky, V.Y., 2017. Adipose HIF-1α causes obesity by suppressing brown adipose tissue thermogenesis. J. Mol. Med (Berl.) 95, 287–297. https://doi.org/10.1007/s00109-016-1480-6.

Kanehisa, M., Goto, S., 2000. KEGG: kyoto encyclopedia of genes and genomes. Nucleic Acids Res 28, 27–30. https://doi.org/10.1093/nar/28.1.27.

Kang, G.-S., Kim, Y.-E., Oh, H.R., Jo, H.-J., Bok, S., Jeon, Y.K., Cheon, G.J., Roh, T.-Y., Chang, Y.-T., Park, D.J., Ahn, G.-O., 2024. Hypoxia-inducible factor-1α-deficient adipose-tissue macrophages produce the heat to mediate lipolysis of white adipose tissue through uncoupling protein-1. Lab Anim. Res 40, 37. https://doi.org/10.1186/s42826-024-00224-4.

Klionsky, D.J., Abdalla, F.C., Abeliovich, H., Abraham, R.T., Acevedo-Arozena, A., Adeli, K., et al., 2012. Guidelines for the use and interpretation of assays for monitoring autophagy. Autophagy 8, 445–544. https://doi.org/10.4161/auto.19496.

Klionsky, D.J., Abdelmohsen, K., Abe, A., Abedin, M.J., Abeliovich, H., Acevedo Arozena, A., et al., 2016. Guidelines for the use and interpretation of assays for monitoring autophagy (3rd edition). Autophagy 12, 1–222. https://doi.org/10.1080/15548627.2015.1100356.

Klusóczki, Á., Veréb, Z., Vámos, A., Fischer-Posovszky, P., Wabitsch, M., Bacso, Z., Fésüs, L., Kristóf, E., 2019. Differentiating SGBS adipocytes respond to PPARγ stimulation, irisin and BMP7 by functional browning and beige characteristics. Sci. Rep. 9, 5823. https://doi.org/10.1038/s41598-019-42256-0.

Lee, Y.-K., Cowan, C.A., 2013. White to brite adipocyte transition and back again. Nat. Cell Biol. 15, 568–569. https://doi.org/10.1038/ncb2776.

Lu, X., Altshuler-Keylin, S., Wang, Q., Chen, Y., Henrique Sponton, C., Ikeda, K., Maretich, P., Yoneshiro, T., Kajimura, S., 2018. Mitophagy controls beige adipocyte maintenance through a Parkin-dependent and UCP1-independent mechanism. Sci. Signal 11, eaap8526. https://doi.org/10.1126/scisignal.aap8526.

Mizushima, N., Yoshimori, T., 2007. How to interpret LC3 immunoblotting. Autophagy 3, 542–545. https://doi.org/10.4161/auto.4600.

Montanari, T., Colitti, M., 2018. Simpson-Golabi-Behmel syndrome human adipocytes reveal a changing phenotype throughout differentiation. Histochem Cell Biol. 149, 593–605. https://doi.org/10.1007/s00418-018-1663-z.

Peng, J.-Y., Lin, C.-C., Chen, Y.-J., Kao, L.-S., Liu, Y.-C., Chou, C.-C., Huang, Y.-H., Chang, F.-R., Wu, Y.-C., Tsai, Y.-S., Hsu, C.-N., 2011. Automatic morphological subtyping reveals new roles of caspases in mitochondrial dynamics. PLoS Comput. Biol. 7, e1002212. https://doi.org/10.1371/journal.pcbi.1002212.

Perdikari, A., Leparc, G.G., Balaz, M., Pires, N.D., Lidell, M.E., Sun, W., Fernandez-Albert, F., Müller, S., Akchiche, N., Dong, H., Balazova, L., Opitz, L., Röder, E., Klein, H., Stefanicka, P., Varga, L., Nuutila, P., Virtanen, K.A., Niemi, T., Taittonen, M., Rudofsky, G., Ukropec, J., Enerbäck, S., Stupka, E., Neubauer, H., Wolfrum, C., 2018. BATLAS: Deconvoluting Brown Adipose Tissue. Cell Rep. 25, 784–797.e4. https://doi.org/10.1016/j.celrep.2018.09.044.

Romero-Corral, A., Somers, V.K., Sierra-Johnson, J., Thomas, R.J., Collazo-Clavell, M.L., Korinek, J., Allison, T.G., Batsis, J.A., Sert-Kuniyoshi, F.H., Lopez-Jimenez, F., 2008. Accuracy of body mass index in diagnosing obesity in the adult general population. Int J. Obes. (Lond.) 32, 959–966. https://doi.org/10.1038/ijo.2008.11.

Shimizu, I., Aprahamian, T., Kikuchi, R., Shimizu, A., Papanicolaou, K.N., MacLauchlan, S., Maruyama, S., Walsh, K., 2014. Vascular rarefaction mediates whitening of brown fat in obesity. J. Clin. Invest 124, 2099–2112. https://doi.org/10.1172/JCI71643.

Speakman, J.R., 2025. Ferroptosis in adipose tissue: A promising pathway for treating obesity? Cell Metab. 37, 560–561. https://doi.org/10.1016/j.cmet.2025.01.029.

Su, R., Dalai, M., Luvsantseren, B., Chimedtseren, C., Hasi, S., 2022. Comparative study of the function and structure of the gut microbiota in Siberian musk deer and Forest musk deer. Appl. Microbiol Biotechnol. 106, 6799–6817. https://doi.org/10.1007/s00253-022-12158-9.

Szatmári-Tóth, M., Shaw, A., Csomós, I., Mocsár, G., Fischer-Posovszky, P., Wabitsch, M., Balajthy, Z., Lányi, C., Győry, F., Kristóf, E., Fésüs, L., 2020. Thermogenic Activation Downregulates High Mitophagy Rate in Human Masked and Mature Beige Adipocytes. Int J. Mol. Sci. 21, 6640. https://doi.org/10.3390/ijms21186640.

Tews, D., Brenner, R.E., Siebert, R., Debatin, K.-M., Fischer-Posovszky, P., Wabitsch, M., 2022. 20 Years with SGBS cells - a versatile in vitro model of human adipocyte biology. Int J. Obes. (Lond.) 46, 1939–1947. https://doi.org/10.1038/s41366-022-01199-9.

Wabitsch, M., Brenner, R.E., Melzner, I., Braun, M., Möller, P., Heinze, E., Debatin, K.M., Hauner, H., 2001. Characterization of a human preadipocyte cell strain with high capacity for adipose differentiation. Int J. Obes. Relat. Metab. Disord. 25, 8–15. https://doi.org/10.1038/sj.ijo.0801520.

Wang, Xue, Wu, Q., Zhong, M., Chen, Y., Wang, Y., Li, X., Zhao, W., Ge, C., Wang, Xinhui, Yu, Y., Yang, S., Wang, T., Xie, E., Shi, W., Min, J., Wang, F., 2025. Adipocyte-derived ferroptotic signaling mitigates obesity. e7 Cell Metab. 37, 673–691. https://doi.org/10.1016/j.cmet.2024.11.010.

Yu, J., Zhang, S., Cui, L., Wang, W., Na, H., Zhu, X., Li, L., Xu, G., Yang, F., Christian, M., Liu, P., 2015. Lipid droplet remodeling and interaction with mitochondria in mouse brown adipose tissue during cold treatment. Biochimica et Biophysica Acta (BBA) Molecular Cell Research 1853, 918–928. https://doi.org/10.1016/j.bbamcr.2015.01.020.